Reynolds effects on wall pressure fluctuations at stall inception of a wind turbine blade section

B. Hanna, C. Braud, Bérengère Podvin, J. Deparday

PAPER • **OPEN ACCESS**

Reynolds effects on wall pressure fluctuations at stall inception of a wind turbine blade section

To cite this article: B. Hanna *et al* 2024 *J. Phys.: Conf. Ser.* **2767** 022052

Journal of Physics: Conference Series **2767** (2024) 022052 doi:10.1088/1742-6596/2767/2/022052

Reynolds effects on wall pressure fluctuations at stall inception of a wind turbine blade section

B. Hanna[1]‡, C. Braud[1,2], B. Podvin[3], J. Deparday[4]

1- CSTB, Centre Scientific et Technique du Bâtiment, Nantes, France
2- Nantes Université, CNRS, Centrale Nantes, LHEEA lab., Nantes, France
3- Univ. Paris-Saclay, CNRS, Centrale Supélec, EM2C lab., Gif-sur-Yvette, France.
4- IET, OST - Eastern Switzerland Univ. of Applied Sc., Rapperswil, Switzerland

Keywords: 2D Blade aerodynamics, Incipient stall, High Reynolds numbers

1. Abstract

Understanding the flow physics over airfoils near stall is of major importance for improvement of dynamic stall models. However, static stall is a first important step that remains challenging. The present study focuses on the influence of Reynolds number on the stall inception of an airfoil, one of the important parameter impacting the stall behavior. The blade, extracted from scans of an operated 2MW turbine, is investigated experimentally at full scale using two chordwise lines of unsteady wall pressure sensors with Reynolds numbers ranging from 5×10^5 to 4.2×10^6. Results reveal an important dependence of the pressure fluctuations with the Reynolds number: their relative level compared with the intrados value is progressively increased with the Reynolds number in the intermittent separation region which corresponds to the peak of pressure standard deviation.

2. Introduction

The stall inception on wind turbine blades can occur either from atmospheric inflow perturbations or from non-optimal operations (yaw misalignment, motions of floating wind turbines, ...), and produce large load fluctuations and fatigue decreasing the lifetime of the wind turbine blades. A better comprehension of the stall inception would improve blade control and provide a better estimation of the aerodynamic loads on the wind turbine blades, essential for optimal blade design. Moreover, wind turbines operate over a large range of Reynolds numbers from stand still to high velocities and intermittent gust. Near stall, the flow becomes more three-dimensional and highly unsteady which induces important load fluctuations ([1,5,7,8]) that are not considered in dynamic stall models. The stall inception is also found to greatly depend on the

‡ corresponding author: badoui.hanna@cstb.fr

Reynolds number. Brunner et al. [2] have investigated experimentally the chord-based Reynolds number effect, Re_c, ranging from 5×10^5 to 7.9×10^6 of a moderately thick airfoil. The stall shifts from trailing-edge stall to leading-edge stall at around $Re_c = 2 \times 10^6$. A wind airfoil with the same shape and size as rotor-blade of a 2MW turbine at 80% of the span has been experimentally studied at high chord-based Reynolds number (4.7×10^6) [7] and at lower Reynolds number O(10^5) [6]. Both Reynolds number ranges exhibit a trailing-edge stall, contrary to what was found for a different airfoil shape by Brunner et al [2].

These recent findings highlight the fact that the stall inception is a complex phenomenon, less understood at high Reynolds number than at lower ones. It is therefore of importance to analyze its evolution with the Reynolds number. In this paper, wall-pressure measurements of a thick cambered airfoil are presented at stall inception for Re_c ranging from 5×10^5 to 4.2×10^6, thus making a bridge between low and high Reynolds studies.

3. Setup

3.1. The CSTB wind tunnel

Experiments were performed in the aerodynamic test section of the climatic Wind tunnel of CSTB at Nantes-France (see figure 1). It is 6m wide, 5m high, and 12m long and has a low blockage about 8% for a blade Chord of 1.25m at AoA = 24°). The wind speed could reach 70 $\frac{m}{s}$, corresponding to a chord-based Reynolds number of $Re_c = 5.9 \times 10^6$ for a chord of 1.25m. The flow uniformity and the turbulence intensity were characterized before the tests by measuring the velocity profiles for 2 minutes per velocity across the test section using several cobra probes sampled at 1024 Hz. The range of the velocity varies from 6 $\frac{m}{s}$ to 43 $\frac{m}{s}$. The turbulence intensity varies between 1.3% to 1.7% independently of the inflow velocity and the span-wise variations of the mean velocity are around 1 to 2 %. The boundary layers on the ground, ceiling, inner and outer both sides were studied carefully for seven velocities ranging from 12 $\frac{m}{s}$ to 54 $\frac{m}{s}$ in the middle of the test section. Its height is about 30 cm on the ground, 25 cm on the ceiling, about 18 cm on the outer side (Y $>$ 0) and between 30 cm and 40 cm on the inner side (Y $<$ 0; where the turbulence level is also higher).

3.2. The airfoil

The blade of a 2-MW commercial wind turbine operated by VALEMO at the Saint-Hilaire de Chaléons site in France has been scanned. The airfoil shape at 80% of the rotor radius has been extracted and extruded in 2D to be installed in the wind tunnel. The maximum thickness, 20%, is located at around 33% of the chord while the maximum camber, 4%, is located at approximately 49% of the chord. Previous studies from [1, 7] have shown that this blade shape has a trailing edge stall behaviour according to Gault's

classification [3]. The airfoil is 5m wide and has the full scale chord length of c = 1.25m. The aspect ratio is thus 4 and the maximum blockage ratio is 8% at 24°.

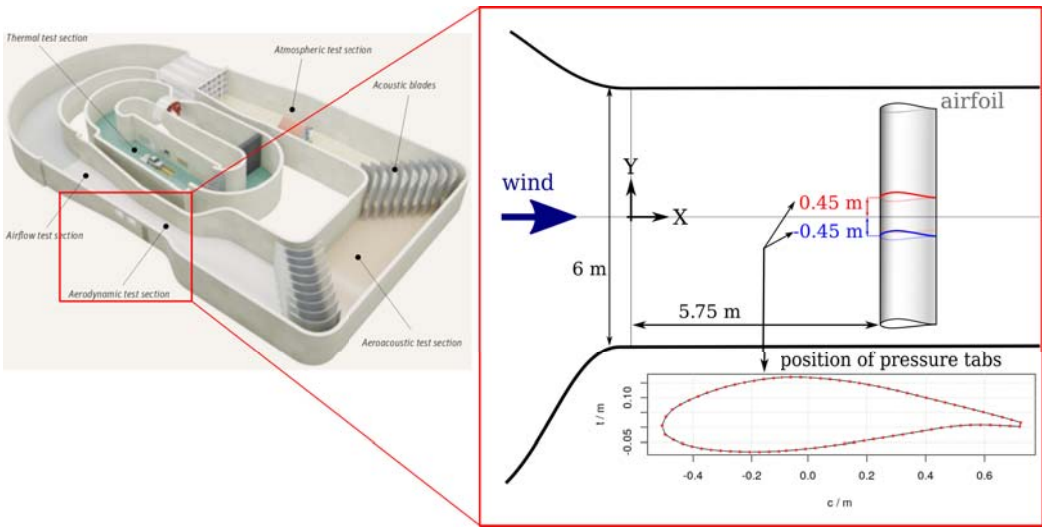

Figure 1. Wind tunnel set-up and airfoil installation.

3.3. The unsteady pressure sensors

This blade is equipped with two rows of 78 unsteady wall pressure taps each in the chord-wise direction, located at two spanwise positions as shown in figure 1. They are equally distributed from the mid-span of the blade ($Y^+ : Y/c = +0.36$ and $Y^- : Y/c = -0.36$). The chord-wise spacing between the pressure taps is 0.026c, where c is the chord of the airfoil. The pressure taps were connected to five multiplexed EPS pressure scanners of 32 channels each, using 1.5 m long vinyl tubes with an internal diameter of 0.8 mm. Two ranges of the pressure sensors were used depending on their location, 0 kPa to 7 kPa near the leading edge suction peak and 0 to 2.5 kPa elsewhere, with a precision of ±0.03% of the full measurement range. The transfer function of the whole system (tubes plus sensor cavity) has been measured off-line at a sampling frequency of 1024 Hz following the methodology of Holmes and Lewis [4] and Whitmore et al. [9]. The signal acquisition was performed using two National Instrument acquisition boards linked by real-time system integration for synchronization purposes. The sampling frequency was 512 Hz and its duration was at least 60 s which was found to be sufficient to have statistical convergence of the mean pressure coefficient C_P and the standard deviation STD(C_P). In order to study the Reynolds effect on the physics of the flow, tests were performed at six chord-based Reynolds numbers, Re_c: 5×10^5, 8.5×10^5, 1.7×10^6, 2.5×10^6, 3.4×10^6 to 4.2×10^6. Pressure measurements at eight positions near the leading edge (see figure 2) are missing due to technical issues for three wind speeds ($Re_c = 5 \times 10^5$, 8.5×10^5 and 4.2×10^6) out of six. For fair comparison, these positions were not included in the computation of the normal force coefficient at all Reynolds

numbers. This prevents the description of the impact on the normal force coefficient which includes the leading-edge suction peak contribution. However, it is sufficient to compare the impact of the Reynolds number taking into account the intermittent separation region. This is justified since the leading edge suction peak does not evolve with the Reynolds number. In Braud et al. [1], this intermittent region was defined by the maximum standard deviation peak in the recovery region.

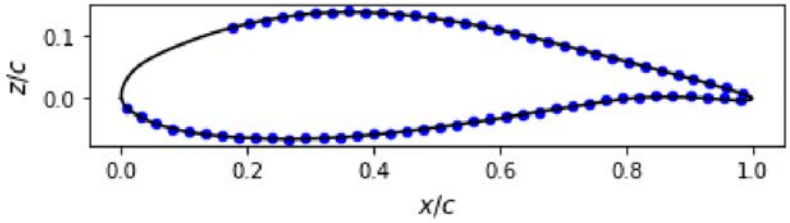

Figure 2. Pressure sensors distribution on the airfoil used to compute the mean and the standard deviation of the normal coefficient, $< C_N >$ and STD(C_N) respectively.

In this study, the normal force coefficient C_N and the pressure coefficient $C_p = \frac{\Delta p}{q_0}$ (with Δp the differential pressure between the wall pressure and the dynamic pressure q_0) were primarily investigated by scanning the angles from -10° to 28°. The mean quantities and the standard deviation are noted respectively $< . >$ and STD(.). The mean normal force coefficient in figure 3 indicates the force normal to the airfoil chord, and was obtained by integrating the mean pressure coefficient around the airfoil. As the lift force is calculated from the normal and tangential forces, and the latter are only partially retrievable from the pressure coefficient (the viscous part of the tangential force was ignored using this measurement method), the present study focuses on the normal force coefficient.

4. Results

4.1. Normal force

Figure 3 shows the mean normal force coefficient without the leading edge suction peak for the six different wind speeds.

The mean normal force coefficients, computed without the leading edge suction peak (see section 3.3), for all Re_c show a typical lift distribution on this wind turbine blade. A linear increase of $< C_N >$ is noticed for angles of attack (AoA) lower than 7°. The maximum of $< C_N >$ is reached at 9° for $Re_c = 5 \times 10^5$ and 8.5×10^5, and occurs at a slightly higher angle of attack, AoA= 11°, for higher Re_c (from $Re_c = 1.7 \times 10^6$). The amplitude of this maximum does not change significantly with the increase of Re_c. In the following, C_N will be analyzed further through its standard deviation value STD(C_N) (see figure 4), as previous studies have highlighted an important increase of it for a given angle of attack [1].

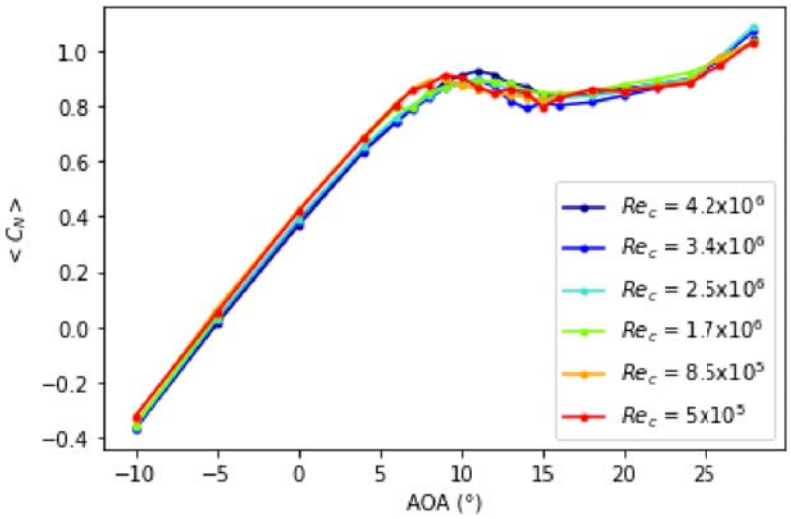

Figure 3. The mean normal force coefficient ($< C_N >$) at the row of pressure Y^+ for different chord-based Reynolds number: Re_c.

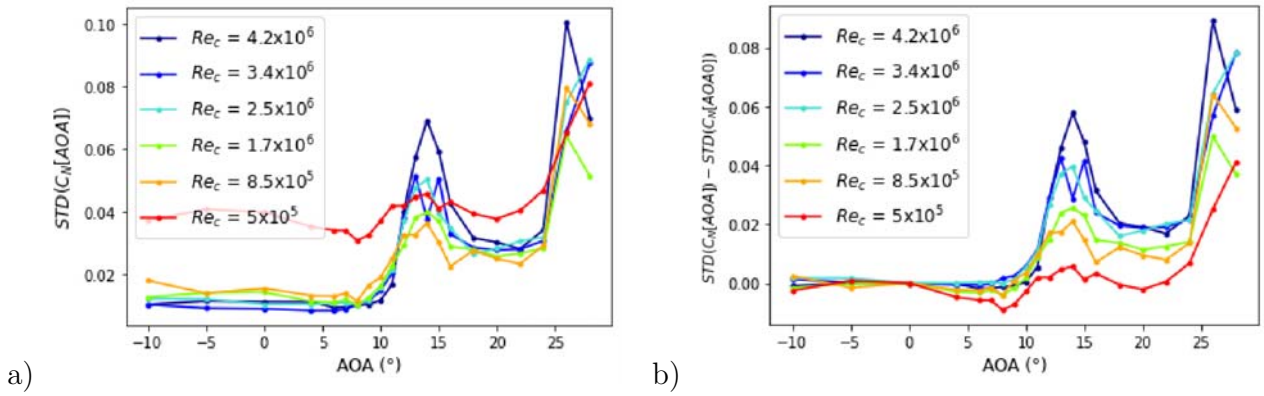

a) b)

Figure 4. Standard deviation (a) and the relative standard deviation (b) of the normal force coefficient ($STD(C_N) - STD(C_N(\text{AOA}=0°))$ at Y^+ spanwise location for different chord-based Reynolds number.

The figure 4a shows the standard deviation of the normal coefficient. It is significantly high at the low Reynolds numbers $Re_c = 5 \times 10^5$ for all angles of attack. However, relatively to the value at 0°, the standard deviation peak level for the AoA ranging from 12° to 16° is progressively increasing with the Reynolds number (figure 4b). Also, the peak is wider at low Reynolds numbers, so that the exact location of its maximum is less obvious. Note that the $Re_c = 3.4 \times 10^6$ case presents a double peak around 14° compared to other Reynolds number cases. The peak occurring at higher angles of attack is to be related to the full flow separation over the suction side, outside of the scope of the present paper.

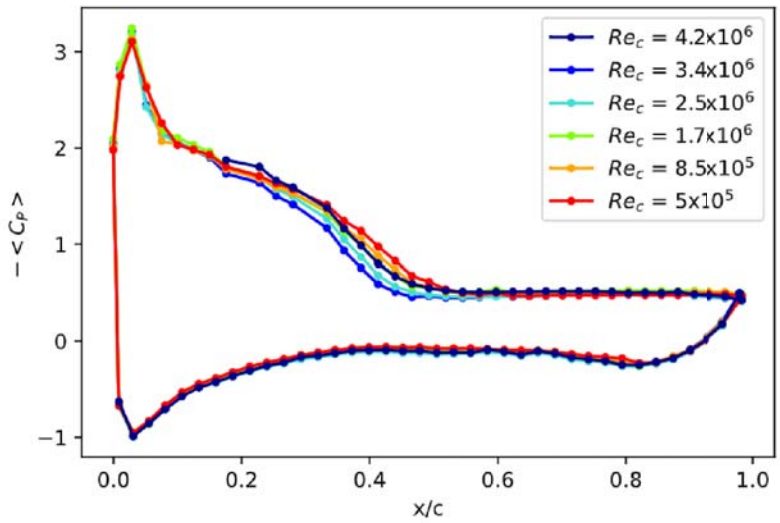

Figure 5. Pressure coefficient distribution (C_P) in chordwise direction x/c, at Y^+ spanwise location and 14° of angle of attack, for different chord-based Reynolds numbers.

4.2. Local force

Now, the spatial distribution of the pressure coefficient (C_P) is examined for the spanwise location at Y^+ at 14°, for which a maximum occurs in the normal force (except for the $Re_c = 3.4 \times 10^6$). The goal here is to show the influence of Re_c on its distribution. From figure 5, the pressure distribution has the same pattern for all Re_c: a peak of pressure coefficient at the leading edge that reaches -3.3, a zone of high suction in the first half of the chord, then a decrease of the suction until the trailing edge also called the recovery region. When the mean pressure distribution reaches a plateau, it indicates the steady separation point location as defined by [1, 7]. While comparing different Re_c, no effect was shown on the leading edge peak in term of its location or its amplitude. However the region of pressure gradient varies with the Reynolds number. For $Re_c = 5.10^5$, this region ends at $\frac{x}{c}$= 0.55 and it moves towards the leading edge with the increase of Re_c reaching $\frac{x}{c} = 0.47$ at $Re_c = 3.4 \times 10^6$. This indicates that increasing the Reynolds number moves the mean separation point towards the leading edge. At $Re_c = 4.2 \times 10^6$, this trend is not followed with a sudden displacement of the mean separation point towards the leading edge. In this region the flow alternates between an attached and separated state and it is not straightforward to prescribe its evolution with the Reynolds number. This highly intermittent region will be further analysed using the standard deviation peak of C_P which was found more representative (see [1])

Figure 6a shows the distribution of the pressure standard deviation in the chordwise direction x/c. The low Reynolds number case presents a global increase of its value over all x/c. To be able to compare the peak evolution in the recovery region with the Reynolds numbers, figure 6b shows its relative value with one point at the pressure side

taken at $\frac{x}{c}$=0.4. This relative standard deviation has the same trend for all Reynolds numbers except for $Re_c = 3.4 \times 10^6$ (related to the double peak observed in the $< C_N >$ curve, see figure 3): a first bump at the leading edge position at the same location for all Re_c (when available), a second bump which maximum is related to the intermittent separation point (see [1]) that significantly increases with the Reynolds number (from 0.075 to 0.24) and is progressively evolving from $\frac{x}{c} = 0.45$ to $\frac{x}{c} = 0.38$. Finally, a third bump is observed in the trailing edge region, related to the separated shear-layer flapping, the amplitude of which is increased with the Reynolds number. To the knowledge of the authors, this is the first time the Reynolds number influence is reported in that intermittent region.

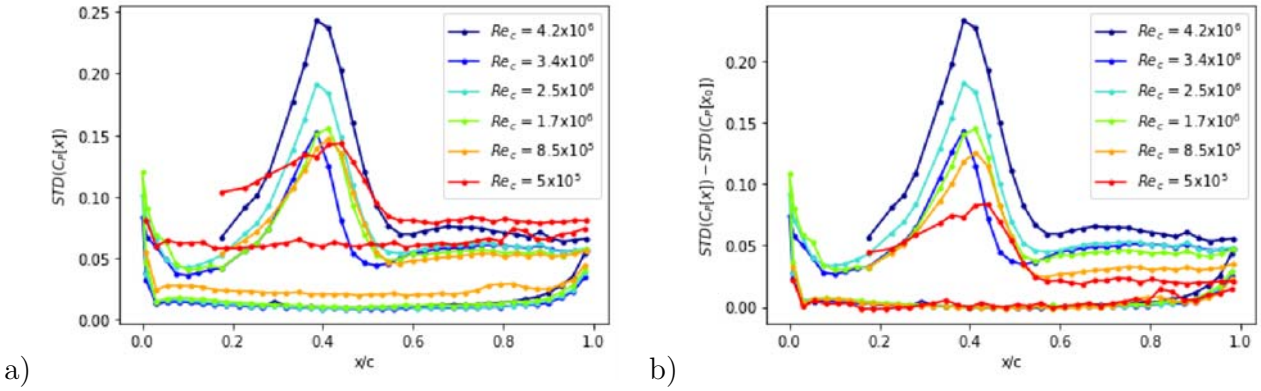

Figure 6. Distribution of the pressure coefficient standard deviation, $STD(C_P)$ (a) and the relative pressure coefficient standard deviation with its value at the pressure side at $\frac{x}{c}$=0.4, $(STD(Cp) - STD(Cp(\frac{x}{c} = 0.4))$ (b), for Y^+ and at 14 °.

4.3. Unsteady pressure signals: bi-stability

At the standard deviation peak on both spanwise locations Y^+ and Y^-, the time signals of the pressure were compared using the cross-correlation. They were found to be highly anti-correlated at 14° [1]. Also, before reaching this maximum anti-correlation value, the level of correlation was found to progressively decrease down to 0 at 10°, just before separation. Figure 7 presents the instantaneous pressure coefficient signals for both rows along the spanwise direction (Y^+ and Y^-), extracted at the position where the maximum standard deviation was found. The instantaneous pressure coefficient signals alternate between 2 states, with opposing phase for both rows of pressure, for all Reynolds numbers. It is similar to the bi-stability phenomenon defined in [1] at a unique Reynolds number. Note that the bi-stability is also found at the peculiar value of the Reynolds number, $Re_c = 3.4 \times 10^6$, with however more low frequencies than other Reynolds cases. The correlation coefficient is computed between the two signals for all Reynolds numbers and reported in table 1. All signals are found to be highly anti-correlated. However, excluding the peculiar Reynolds number case, $Re_c = 3.4 \times 10^6$, this anti-correlation value is decreasing with the Reynolds number. This is in good

agreement with previous observations of the intermittent separation region, where the pressure fluctuations are decreasing with the Reynolds number.

Table 1. Cross-correlation coefficients between Y^+ and Y^- pressure coefficient signals at their maximum standard deviation location for the angle of attack of 14 °.

Re_c	1.7×10^6	2.5×10^6	3.4×10^6	4.2×10^6
Correlation	-0,655	-0,768	-0,541	-0,849

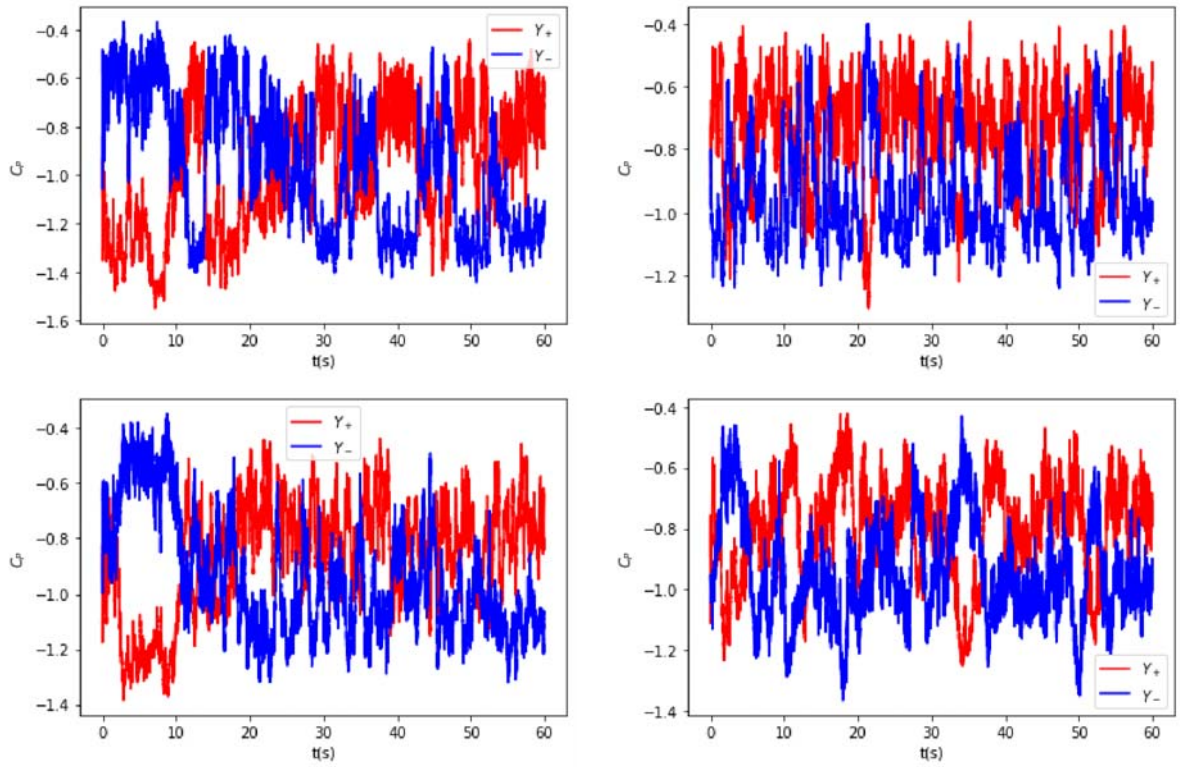

Figure 7. Signal of the pressure coefficient at its maximum relative standard deviation for Y^+ and Y^- in red and blue respectively at top left: $Re_c = 4.2 \times 10^6$; top right: $Re_c = 3.4 \times 10^6$; bottom left: $Re_c = 2.5 \times 10^6$; bottom right: $Re_c = 1.7 \times 10^6$

5. Conclusions/Perspectives

The highly intermittent flow is studied over an airfoil shape corresponding to the 2D extrusion of a 2MW turbine at 80% of the rotor diameter. Evidence of intermittent flow separation and reattachment near maximum lift conditions was first provided by Neunaber et al [7] at a full scale chord-based Reynolds number of $Re_c > 3 \times 10^6$. In the present study, the influence of the Reynolds number was determined on the intermittency phenomenon by considering a wide range of chord-based Reynolds numbers Re_c from

3×10^5 to 4.2×10^6. It was found that the peak of the mean normal coefficient $< C_N >$ is not influenced by Re_c value but that its position increased for a slightly higher angle of attack. The first results at a fixed angle of attack, 14°, near the maximum lift value, showed a non-monotonic evolution of the wall pressure fluctuation peak at mid-chord, where the intermittent region was present. In general, this fluctuation peak value increases with Re_c and moves toward the leading edge over the range of Reynolds numbers considered, while the anticorrelation between the signals at the two spanwise locations that characterizes the intermittent phenomenon becomes stronger. We note that a different behaviour was observed at $Re_c = 3.4 \times 10^5$ and will be investigated in more detail in future experimental studies. The new campaign will include additional wall pressure sensors (in the transverse direction) and load sensors to further characterise the Reynolds number impact on the intermittency in association with global loads.

References

[1] C. Braud, B. Podvin, and J. Deparday. Study of the wall pressure variations on the stall inception of a thick cambered profile at high reynolds number. *Physical Review Fluids*, 2024.

[2] C. E. Brunner, J. Kiefer, M. O. L. Hansen, and M. Hultmark. Study of Reynolds number effects on the aerodynamics of a moderately thick airfoil using a high-pressure wind tunnel. *Experiments in Fluids*, 62(178), 2021.

[3] D. E. Gault. A correlation of low-speed airfoil-section stalling characteristics with reynolds number and airfoil geometry. Technical Report Technical note 3963, National Advisory Committee for Aeronautics, 1957.

[4] J. D. Holmes and R. E. Lewis. The dynamic response of pressure-measurement systems. Auckland, 8-12 December 1986. 9th Australasian Fluid Mechanics Conference.

[5] M. Manolesos, G. Papadakis, and S. G. Voutsinas. Experimental and computational analysis of stall cells on rectangular wings. *Wind Energy*, 17:939–955, 2014.

[6] R. Mishra, I. Neunaber, E. Guilmineau, and C. Braud. Wind tunnel study: is turbulent intensity a good candidate to help in bypassing low reynolds number effects on 2d blade sections? *J. Phys.: Conf. Ser.*, 2265(022095), 2022.

[7] I. Neunaber, F. Danbon, A. Soulier, D. Voisin, E. Guilmineau, P. Delpech, S. Courtine, C. Taymans, and C. Braud. Wind tunnel study on natural instability of the normal force on a full-scale wind turbine blade section at reynolds number 4.7×10^6. *Wind Energy*, page 1-11, 2022.

[8] D. Ragni and C. Ferreira. Effects of 3D stall-cells on the pressure distribution of a laminar NACA64-418 wing. *Experiments in Fluids*, page 57:127, 2016.

[9] S. A. Whitmore, B. J. Petersen, and D. D. Scott. A dynamic response model for pressure sensors in continuum and high knudsen number flows with large temperature gradients. Technical Report Technical Memorandum 4728, NASA, 1996.